Journal of Magnetic Resonance 196 (2009) 33–38

Contents lists available at ScienceDirect

Journal of Magnetic Resonance

journal homepage: www.elsevier.com/locate/jmr

Current density imaging sequences with separation of mobile-ion current from immobile-ion current

Igor Serša *

Jožef Stefan Institute, Jamova 39, 1000 Ljubljana, Slovenia

ARTICLE INFO

Article history:
Received 11 June 2008
Revised 26 September 2008
Available online 2 October 2008

Keywords:
Current density imaging
Charge mobility
Alternating current
Multi spin-echo imaging sequences

ABSTRACT

Three sequences for electric current density imaging (CDI) are studied by testing their ability to selectively detect the electric current of different types of charge carriers. Two of the methods are standard DC-CDI and AC-CDI sequences, and a new AC–DC-CDI sequence is also introduced. The methods rely on the application of square voltage pulses in combination with refocusing RF pulses that can, depending on their position with respect to the voltage pulses, eliminate resistive, capacitive or neither of the current components from the detection pathway. It is demonstrated by experiments on a model system that the DC-CDI sequence detects only the resistive current of mobile ions, the AC–DC-CDI sequence detects only the capacitive current of fixed ions, while the AC-CDI sequence detects both current components. The three sequences introduce a new MRI contrast mechanism that depends on the ion mobility of the sample. As such, the methods may play an important role in the study of electric conductivity phenomena in biological systems.

1. Introduction

MRI is very versatile and one of its emerging applications is current density imaging (CDI). Current density can be imaged in conductive samples containing protons in a liquid. The principle of CDI is based on detecting the magnetic field caused by a current. The current distribution can then be calculated from a map of the detected field change using Ampere's law. The field change is proportional to the frequency shift so it can be mapped by chemical shift imaging methods [1]. If currents are applied in pulses synchronized with an imaging sequence, which is more commonly the case, the field change is proportional to the phase shift [2]. Alternatively, the current distribution can be imaged by detecting small sample displacements that occur due to magnetic forces caused by current flowing through a sample [3]. The group of CDI methods that utilize current detection by magnetic field change can be further divided into direct current density imaging methods (DC-CDI) [2,4], alternating current density imaging methods (AC-CDI) [5] and radiofrequency current density imaging methods (RF-CDI) [6]. As the electrical conductivity of a sample is usually frequency-dependent, all three groups of methods produce different results. The difference occurs due to capacitive currents whose contribution to the sample conductivity increases with increasing frequency, whereas resistive currents do not change with frequency. Such behavior is typical for biological samples where it is known that tissue conductivity increases with increasing frequency [7,8].

Applications of CDI include: technology, where CDI can be used to follow electro-osmotic flow [9,10] or to study electric currents in models of porous materials [11,12]; chemistry, where CDI can be used to monitor chemical reactions that release ions [13]; forestry, where living conditions of trees are associated with the level of potassium ions and with it related conductivity [14]; and biology and medicine, where wide spread applications may be found. A few of these applications are defibrillation [15], electroporation [16], bone fracture healing by currents [17], studying electrically induced skin burns [18], specific radiofrequency absorption rate (SAR) distribution measurements [19] and studying brain conductivity changes during transcranial stimulation [20] or spreading depression [21]. Additionally, CDI has become a complimentary method in the verification and development of new electrical impedance tomography (EIT) methods [22,23].

In this paper, it is demonstrated by experiments on a model system that CDI methods can be designed to separate mobile-ion current from immobile-ion current to image both current components selectively. Two already known CDI methods (DC-CDI and AC-CDI) and one new CDI method (AC–DC-CDI), which is first presented in this paper, are compared by their current-type selectivity. It is theoretically analyzed and experimentally verified that the DC-CDI method detects only the resistive current of mobile ions, the AC–DC-CDI method detects only the capacitive current of fixed ions, while the AC-CDI method detects both current components.

* Fax: +386 1 477 3191.
E-mail address: igor.sersa@ijs.si

1090-7807/$ - see front matter © 2008 Elsevier Inc. All rights reserved.
doi:10.1016/j.jmr.2008.09.026

2. Theory

Electrical properties of biological tissues can be modeled by an electric circuit consisting of two parallel current paths, one for resistive current of mobile ions and the other for capacitive current of fixed ions [5,7]. The circuit consists of a resistor R_m (representing mobile-ion current) to which a resistor R_f with a capacitor C in series (representing fixed-ion current) are connected in parallel (Fig. 1a). Due to its capacitance, the circuit has nonlinear current response to voltage. In the case of an applied square voltage pulse of amplitude V_0 and duration t_1, the current is greatest at the pulse start ($I_{max} = V_0(1/R_m + 1/R_f)$), when the capacitor is empty, and then decreases exponentially with a time constant $\tau = R_fC$ towards the equilibrium resistive current $I_{eq} = V_0/R_m$. Resistive current stops when the voltage pulse has finished. However, capacitive current still flows in the reversed direction as the capacitor, which is still charged, is discharging. Current response of the circuit to the square voltage pulse can be expressed by the equation

$$I(t) = \begin{cases} \frac{V_0}{R_m} + \frac{V_0}{R_f}\exp\left(-\frac{t}{R_fC}\right); & 0 < t < t_1 \\ -\frac{V_0}{R_f}\exp\left(-\frac{t}{R_fC}\right); & t > t_1 \end{cases} \quad (1)$$

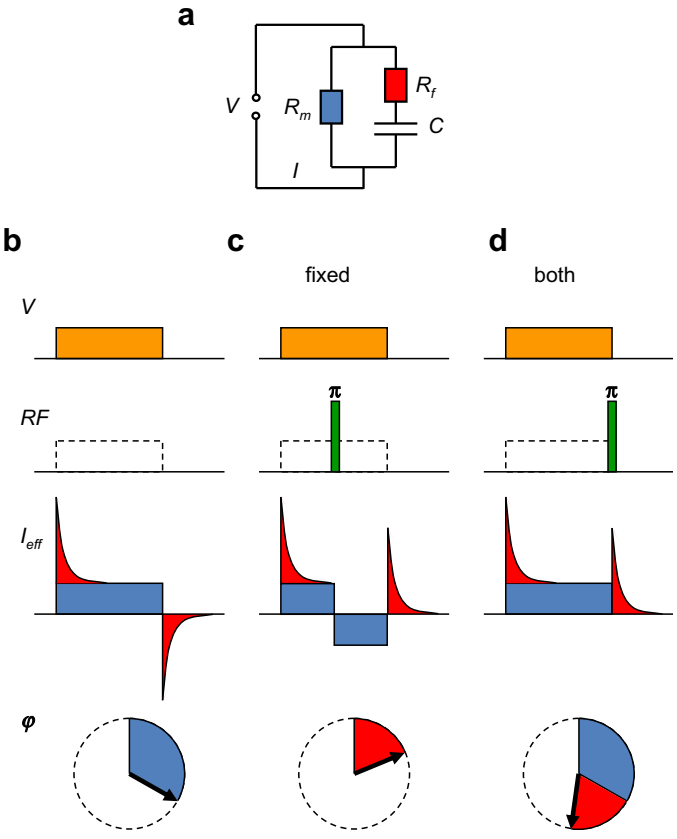

Fig. 1. Current response of the electric circuit consisting of a capacitor C and a resistor R_f in series with a shunt resistor R_m (a) to a square voltage pulse (yellow). It consists of a constant resistive (blue) and exponentially decaying capacitive (red) current. In the pulse sequence (b–d), the effect of the current can be altered by a refocusing RF pulse so that the accumulated phase, induced by the current, is the same as if an effective current I_{eff} were flowing. The accumulated phase is proportional to the resistive current of mobile ions (b) if no refocusing RF pulse is used, to the time average of the capacitive current of fixed ions (c) if the refocusing RF pulse is applied in the centre of the voltage pulse, and to both current components (d) if the refocusing RF pulse is applied immediately after the voltage pulse.

Here is assumed that the capacitor C is fully charged by the end of the voltage pulse, i.e., $t_1 \gg \tau$, and that the circuit is connected to a voltage amplifier with a low output impedance (significantly lower than the circuit impedance).

Most CDI techniques are based on calculating the current density from phase maps of the phase accumulated due to the magnetic field change induced by currents flowing through the sample. The accumulated phase can be reversed at any time in the sequence by applying a refocusing RF pulse. An identical effect can be obtained by applying an effective current which is equal to the actual current (as given by Eq. (1)) that reverses direction each time the refocusing RF pulse is applied. This introduces the possibility of designing different CDI sequences that may enhance the effect of resistive current and suppress the effect of capacitive current or vice versa. Three typical situations are presented in Fig. 1b–d.

The sequence which detects only resistive current (Fig. 1b) consists of just one long voltage pulse without any refocusing RF pulse. Since the accumulated phases of capacitive current at the pulse start and end are equal in magnitude but opposite in sign, the net accumulated phase is then proportional to just to the resistive current. In the second case the voltage pulse is combined with the refocusing RF pulse, which is in the middle of the voltage pulse. The accumulated phase of resistive current is then zero, while the accumulated phase of capacitive current at the pulse start and end are summed (Fig. 1c). The net accumulated phase is then proportional to the time average of the effective capacitive current. In the third case the refocusing RF pulse is applied at end of the voltage pulse, and the accumulated phases of resistive current and capacitive current at the pulse start and end are summed (Fig. 1d). The net accumulated phase is then proportional to the time average of the effective resistive and capacitive current. The following equation expresses the average effective current induced by the voltage pulse of amplitude V_0 and duration t_1 for the three different cases assuming that the capacitive current decay time constant is much less than the duration of the voltage pulse ($R_fC \ll t_1$)

$$\bar{I}_{eff} = \begin{cases} \frac{V_0}{R_m}; & \text{voltage pulse only (DC-CDI)} \\ \frac{2V_0C}{t_1}; & \pi \text{ RF pulse centered to the voltage pulse (AC—DC-CDI)} \\ \frac{V_0}{R_m} + \frac{2V_0C}{t_1}; & \pi \text{ RF pulse at the end of the voltage pulse (AC-CDI)} \end{cases} \quad (2)$$

Since the decay of capacitive current is usually fast, the accumulated phase of capacitive current that is induced by just one voltage pulse may not be enough for successful current density detection. Therefore, it is necessary to accumulate the phase over a large number of short voltage pulses of which phases, induced by capacitive currents, are summed. Each voltage pulse induces capacitive current and with it an associated phase shift. These are accumulated over the whole sequence if the refocusing RF pulses are positioned properly relative to the voltage pulses (Fig. 1c and d). As can be seen from Eq. (2), shorter voltage pulses of alternating polarity, i.e., an AC current of higher frequency, result in a greater time average of the effective capacitive current, and so the detection of the capacitive current density is more efficient.

3. Materials and methods

The correctness of the presented theory for current-type selective CDI was verified on a test sample (Fig. 2) made of two concentric plastic cylinders that were filled with 1.5% saline. The inner cylinder was 13 mm long and 4 mm in diameter, while the outer cylinder was 10 mm in diameter. The inner cylinder with a resistance of $R_s = 0.5\ k\Omega$ (measured at 50 Hz) was capped with elec-

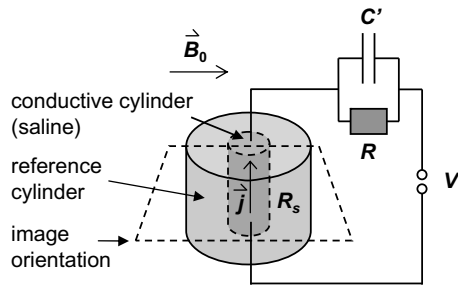

Fig. 2. The model sample consisted of two concentric cylinders filled with saline of which the outer one was used as a reference and the inner one was connected through a capacitor C with a shunt resistor R to the voltage amplifier. The sample was designed to enhance the capacitive current effect of a typical current response of biological samples to voltage pulses. The average current density through the sample was imaged in an orientation perpendicular to the cylinder axis.

trodes at both ends and was connected to a voltage amplifier capable of generating square-shaped electric pulses of positive or negative polarity with an amplitude of $V_0 = 10$ V, while the outer cylinder was used as a reference and was not connected to the amplifier. A capacitor ($C' = 0.33$ μF) with a shunt resistor ($R = 1.3$ kΩ) was connected in series between the power supply and the sample to mimic a situation typical for biological systems where mobile ions (electric current through the resistor) as well as fixed ions (electric current through the capacitor) contribute to electric current. The voltage pulses generated square current pulses with transition spikes (Fig. 1) through the inner cylinder in the axial direction. The current through the sample was monitored by an oscilloscope that measured the voltage drop on a small (1 Ω) resistor connected in series between the amplifier and the sample. The amplifier was controlled by TTL pulses from the spectrometer so that the electric pulses could be synchronized with the imaging sequence and positioned precisely relative to the refocusing RF pulses. The sample was inserted in the MRI magnet with the cylinder axis, i.e., the direction of electric currents, perpendicular to the static magnetic field. Experiments were performed on a 2.35 T horizontal bore Oxford (Abingdon, Oxfordshire, UK) superconducting magnet equipped with Bruker (Ettlingen, Germany) accessories for MR microscopy and a TecMag (Houston, TX, USA) spectrometer. MR images were processed by a TecMag NTNMR and ImageJ (National Institute of Health, USA) image processing software.

The circuit model of the biological tissue in Fig. 1a is somewhat different than the circuit of the test sample in Fig. 2. The resistor R_f in the tissue model is connected in series to the capacitor C and both are connected in parallel to the resistor R_m; in the CDI experiment on the test sample R_f is replaced by the sample resistance R_s, which is connected in series to the capacitor C' and resistor R which are connected in parallel. However, both circuits have identical electrical properties (identical current response to a voltage pulse) when $R_m = Rf$, $R_f = R_s f$ and $C = C'/f^2$ where $f = 1 + R_s/R$. Using these conversions, Eqs. (1) and (2) may be applied to the test sample circuit, resulting in the following "tissue circuit" parameters: $R_m = 1.8$ kΩ, $R_f = 0.69$ kΩ and $C = 0.17$ μF.

Three CDI sequences were tested: the direct current sequence (DC-CDI), the alternating minus direct current sequence (AC–DC-CDI), and the alternating current sequence (AC-CDI). The DC-CDI sequence (Fig. 3a) is based on the conventional spin-echo imaging sequence to which two electric pulses of opposite polarity and total duration t_c are added; one before the refocusing RF pulse and the other after it. The AC–DC-CDI sequence and the AC-CDI sequence (Fig. 3b and c) have the period between the RF excitation and the signal acquisition filled with a train of refocusing RF pulses and short electric pulses. The train consists of an odd number (N) of

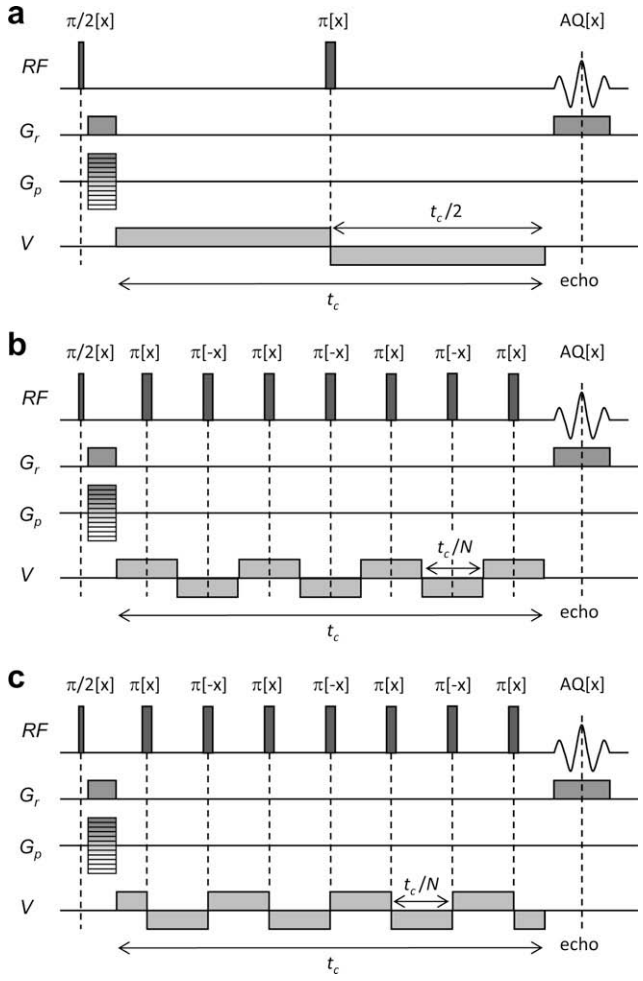

Fig. 3. Three different CDI sequences that differ in their current-type selectivity: DC-CDI sequence (a) that detects only the resistive current of mobile ions, AC–DC-CDI sequence (b) that detects only the capacitive current of fixed ions, and AC-CDI sequence that detects both current components. The sequences, with implemented current-type selectivity principle (presented in Fig. 1), differ in the number and positioning of refocusing RF pulses relative to voltage pulses.

equally spaced RF pulses with total duration t_c that are in the centre of (AC–DC-CDI sequence, Fig. 3b) or followed by (AC-CDI sequence, Fig. 3c) electric pulses of width $t_1 = t_c/N$. The polarity of the electric pulses alternates so that alternating current with a period of $2t_c/N$ flows through the sample. To improve the stability of the sequence, both sequences (AC–DC-CDI and AC-CDI) use phases of the refocusing RF pulses alternating between the $[x]$ and $[-x]$ phase [5,24]. Due to the cylindrical symmetry of the test sample, selection of the imaging slice was not needed. Therefore, the sequences did not include slice selection gradients or shaped RF pulses. The sample was imaged in an orientation perpendicular to the cylinder axis (current direction, Fig. 2) with a field of view of 20 mm and an image matrix of 256 × 256 points. In all CDI sequences the echo time, i.e., the time between the excitation and the acquisition centre, was 25 ms, the repetition time was 1000 ms, the total duration of electric pulses was equal to $t_c = 20$ ms and the duration of hard RF pulses was 9 μs and 18 μs for the excitation and refocusing RF pulses respectively. The DC-CDI sequence consisted of two electric pulses of 10 ms, while the AC–DC-CDI and AC-CDI sequences had $N = 21$ electric pulses of $t_1 = 0.95$ ms each.

The CDI sequences in Fig. 3 accumulate a phase shift φ that is proportional to the time integral of the static magnetic field change

B_c caused by the effective current I_{eff} (Eq. (1), Fig. 1). Each refocusing RF pulse in the sequences in Fig. 3 reverses the sign of the accumulated phase. As each refocusing RF pulse is accompanied by the electric pulse sign change the total accumulated phase is equal to the phase accumulated in the single RF-electric pulse event multiplied by the number of events (N) in the sequence

$$\varphi = N\gamma \int_0^{t_c/N} B_c(t)dt. \quad (3)$$

From the acquired maps of the magnetic field change for all three spatial components, i.e., B_{c_x}, B_{c_y}, and B_{c_z}, the current density can be calculated using Ampere's law $\bar{J} = 1/\mu_0 \nabla \times \bar{B}_c$. The procedure, described in detail in [2,4], involves sample rotation to perpendicular orientations, such that the static magnetic field direction is aligned with the direction of the measured magnetic field change component. The field change maps are then calculated from the phase shift maps using Eq. (3), and finally the current density is calculated. The calculated current density corresponds to the time average of the effective current density. This is equal to the resistive current density if the DC-CDI sequence is used, the time average of the capacitive current density if the AC–DC-CDI sequence is used, and the sum of both current density components in the case of the AC-CDI sequence.

The CDI experiment is significantly simplified if the sample is cylindrically symmetric and current flows along the axis of symmetry. Suppose that the x-axis is the current direction as well as the symmetry axis. The current density j_x is then calculated from the B_{c_y} and B_{c_z} magnetic field change maps using the relation $j_x = 1/\mu_0(\partial B_{c\_z}/\partial y - \partial B_{c\_y}/\partial z)$, where the B_{c_y} map is, due to the cylindrical symmetry of the sample, identical to the B_{c_z} map rotated by 90° around the symmetry axis. Therefore, for the test sample in Fig. 2 as well as for any other sample with a cylindrical symmetry, no sample rotation is needed to acquire a field change map of the perpendicular component.

4. Results

The test sample in Fig. 3 had a time-dependent current response to square-shaped voltage pulses. The current was greatest at the pulse start when the capacitor C was empty and, in addition to resistive current, capacitive current was flowing and charging the capacitor. As the capacitor was charging, the current decreased

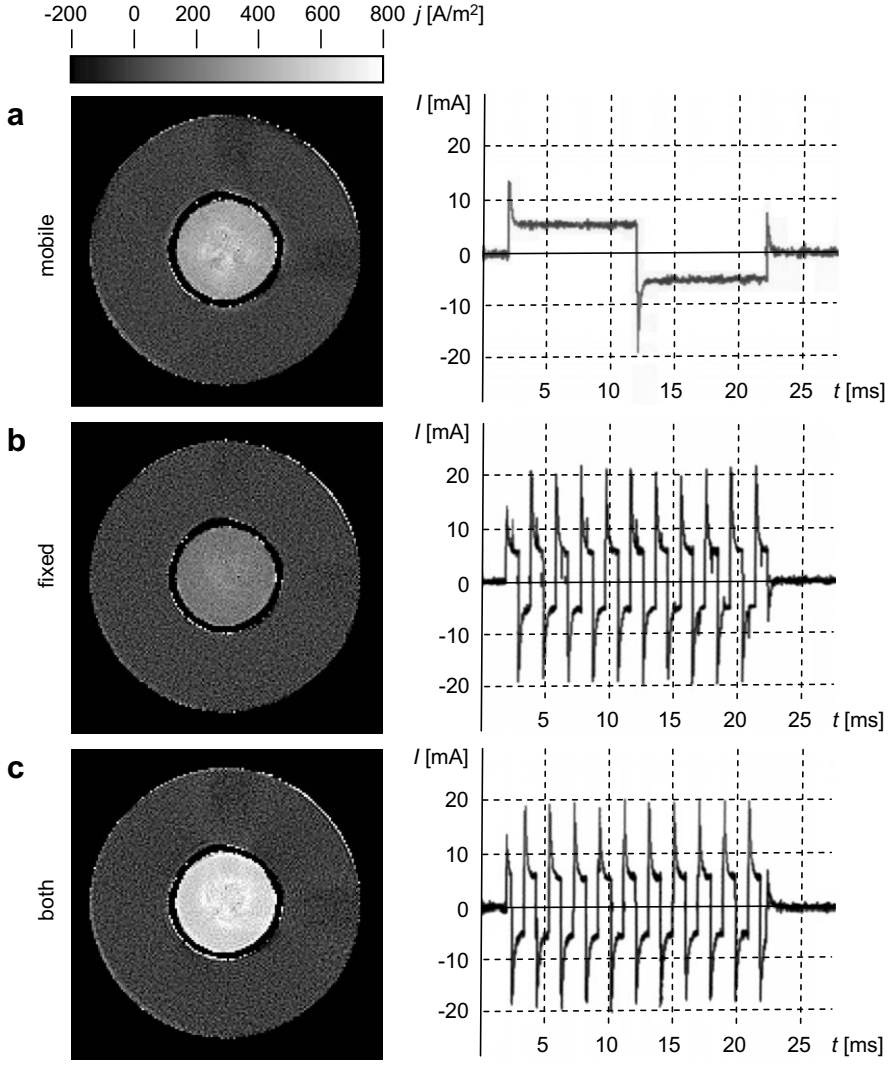

Fig. 4. Measured current through the sample (right) and corresponding measured average current density through the test sample for three CDI sequences differing in current-type selectivity (left). The DC-CDI sequence (a), which detects only resistive current of mobile ions, the AC–DC-CDI sequence (b), which detects only capacitive current of fixed ions, and the AC-CDI sequence (c), which detects both capacitive and fixed-ion currents. The sum of the average current densities for the DC-CDI (420 A/m^2) and AC–DC-CDI (210 A/m^2) sequences corresponds well with the average current density of the AC-CDI sequence (600 A/m^2).

exponentially to equilibrium with a decay constant $\tau = R_f C = 0.69\ \text{k}\Omega\ 0.17\ \mu\text{F} = 0.12$ ms. After the pulse, the current direction reversed due to the capacitor discharging. The discharge current decreased exponentially to zero with the same decay constant of 0.12 ms.

The current response of the sample to square voltage pulses in different pulse sequences can be seen in Fig. 4. In the DC-CDI sequence (Fig. 4a) with only two voltage pulses the capacitive current effect was negligible. During both voltage pulses, i.e., in period t_c, the current was practically constant and equal to the resistive current of $V_0/R_m = 10\ \text{V}/1.8\ \text{k}\Omega = 5.5$ mA. The AC–DC-CDI and AC-CDI sequences (Fig. 4b and c) both consisted of many short voltage pulses ($N = 21$, $t_1 = t_c/N = 0.95$ ms) during which the current was unsteady and, due to transition phenomena, significantly larger in average than the resistive current. The initial current at the pulse start was more than twice as big as the resistive current. The current was approximately 12 mA at the start of the first and the end of the last pulse in the sequence and was twice as big for other pulses due to the overlap of discharge and recharge currents that co-add due to the reversed polarity of two neighboring voltage pulses.

The measured current densities in different CDI sequences depended on the current response of the sample to the voltage pulses and also on the position of the RF refocusing pulses in the sequence relative to the voltage pulses. In the DC-CDI sequence the steady resistive current of mobile ions through the inner cylinder of the sample produced a quasi-static magnetic field that resulted in an accumulated phase that increased linearly with time. The corresponding current density, calculated from the phase map, was $420 \pm 60\ \text{A/m}^2$ in the inner cylinder and zero in the outer one (Fig. 4a). In the AC–DC-CDI and AC-CDI sequences current was unsteady; a boxed current envelope of resistive current was accompanied by a transient exponentially decaying capacitive current at the voltage pulse start and end. Due to the symmetric positioning of the refocusing RF pulses relative to the voltage pulses in the AC–DC-CDI sequence (Fig. 4b), accumulated phases of resistive current in intervals before and after refocusing RF pulses were cancelled out. Thus, the net accumulated phase, and the resulting calculated current density of $210 \pm 60\ \text{A/m}^2$, was proportional to only the time average of the capacitive current. In the AC-CDI sequence (Fig. 4c) the refocusing RF pulses were between voltage pulses. This arrangement of refocusing RF pulses preserved the accumulated phase of the resistive and the capacitive current. The calculated current density of $600 \pm 60\ \text{A/m}^2$ corresponds well with the sum of the calculated resistive (Fig. 4a) and capacitive (Fig. 4b) current densities. In all three experiments no current was detected in the outer reference cylinder.

The measured current densities of the three CDI sequences can be multiplied by the cross-sectional area of the inner cylinder ($13\ \text{mm}^2$) and so converted into average effective currents flowing through the test sample. This yields inner cylinder currents of 5.5 mA, 2.7 mA and 7.8 mA for the DC-CDI, AC–DC-CDI and AC-CDI respectively. The currents are in a reasonable agreement with the theoretical values given by Eq. (2) which correspond to 5.5 mA, 3.6 mA and 9.1 mA.

5. Discussion

Interestingly, the sum of the average current densities for the DC-CDI ($420\ \text{A/m}^2$) and AC–DC-CDI ($210\ \text{A/m}^2$) sequences is within the experimental error ($60\ \text{A/m}^2$) of the measured current density for the AC-CDI sequence ($600\ \text{A/m}^2$). This result confirms the current-type selectivity of the three CDI sequences. Somewhat bigger discrepancy between experimental and theoretical vales for the average effective current through the inner cylinder (2.7 mA vs. 3.6 mA for the AC–DC-CDI sequence and 7.8 mA vs. 9.1 mA for the AC-CDI sequence) may be due to stability problems of multi spin-echo sequences with auxiliary phase encoding [25] and incomplete decay of the capacitive current before execution of the refocusing RF pulse in each voltage/RF pulse pair.

The sample used for demonstrating the current-type selectivity of the CDI sequences consisted of an external capacitor with a shunt resistor connected in series to a saline sample (Fig. 2) to enhance and simulate the effect of fixed-ion current. In a regular CDI experiment, a sample is placed between two electrodes and no external circuit for fixed-ion current enhancement is used. The ratio between mobile-ion (resistive) and fixed-ion (capacitive) current in that case depends on dielectric and conductive properties of the sample, on the electrode geometry and arrangement as well as on the capacitance due to the electrode/tissue interface. The electrical properties of the sample can be described by the electrical circuit in Fig. 1a with a parallel-plate capacitor of capacitance $C = \varepsilon\varepsilon_0 A/d$, a mobile-ion resistance by $R_m = \rho d/A$, and a fixed-ion resistance by $R_f = \tau/C$. Here ε is the sample dielectric constant, ε_0 is the permittivity of free space, A is the electrode area, d is the distance between the electrodes, ρ is the sample resistivity and τ is the sample dielectric relaxation time. In most samples, especially biological ones, sample conductivity is low (a typical biological tissue has approximately ten times lower DC conductivity than the saline sample used in the presented experiment) and the use of high voltage, i.e., several hundred volts, is inevitable in order to detect current by CDI. High voltage increases not only resistive current but also capacitive, i.e., fixed-ion current. However, exceedingly high voltage may lead to sample damage and cannot be applied to living systems. Fixed-ion current may also be increased by increasing the electrode area A and by decreasing the distance between the electrodes d. In addition to biological applications of the presented CDI sequences, where sample conductivity may be the limiting factor, there are many applications of the method in electrochemistry [26] where imaging different current-type components in ionic solutions may be of interest. Ionic solutions usually have sufficient conductivity and are less susceptible to damage associated with the use of high voltage. The applications may range from batteries and fuel cells, chemical reactions that release ions to electro-osmotic flow systems.

The average fixed-ion current can also be increased in AC–DC-CDI and AC-CDI sequences by shortening the voltage pulse widths (Eq. (2)), i.e., by increasing the alternating current frequency. Ideally, the pulse width t_c/N should be of the same order as the dielectric relaxation time. Sophisticated analysis of dielectric and conductivity properties of various biological tissues by the 4-Cole-Cole function yields four characteristic dielectric relaxation times that correspond to different frequency regimes [7]. These four times are on the order of, from longest to shortest: 10 ms, 100 μs, 100 ns and 10 ps. In CDI experiments the shortest voltage pulse width is limited by the shortest possible refocusing RF pulse separation. In living systems this is limited by SAR, whereas no such limits exist in model or in-vitro systems where voltage pulse widths can easily go below 1 ms thus achieving a frequency of more than 1 kHz AC. In the low frequency range (1–10 kHz) conductivity increase compared to the zero frequency range (below 50 Hz) is for most biological tissues modest and ranges from about 10% (fat), 20% (muscle, heart, liver) to 40% (bone) [27]. A much greater increase would be obtained at frequencies above 100 MHz, where capacitive current prevails. However, currents of such frequencies are undetectable by either of the AC current density methods; they are detectable by the RF-CDI method [6], which is another CDI modality.

The DC-CDI sequence is not exactly a DC sequence as it consists of two electric pulses of opposite polarity with a refocusing RF

pulse in between. It would be more correct to use just one electric pulse with a duration of the two electric pulses, but then it would not be possible to apply the refocusing RF pulse in the middle of the sequence and still accumulate the phase of the two electric pulse halves. Such a single pulse gradient-echo version of the CDI sequence is possible. However, it would lose too much signal in comparison with its spin-echo counterpart.

The presented CDI sequences (Fig. 3) did not use any slice selection, which was reasonable as the sample had symmetry along the cylinder axis, i.e., along the direction perpendicular to the imaging plane. A sample without such symmetry would require slice selection. Use of slice selection through the sample centre would also reduce a small artifact in current density images of the test sample in Fig. 4. The artifact appeared as a region of bright spots in the central region of the inner cylinder, and is most likely due to the electrode RF shielding and susceptibility differences between the electrode and the sample. The effects are significant in proximity of the electrodes and diminish in the central sample region. The artifact could appear also due to incomplete rotational symmetry of the sample; in CDI computation sample images in orientations around rotational symmetry axis are assumed identical. There are several ways of upgrading the sequences with slice selection. Probably the easiest and most efficient method would be the replacement of the excitation RF pulse with a shaped RF pulse combined with a corresponding slice selection gradient. This could increase the time interval between the excitation and the first refocusing RF pulse to some extent. However, this is not really a problem as the time interval does not need to equal half of the time interval between successive refocusing RF pulses (as is the case in the regular CPMG sequence [28]). It only needs to equal the time interval between the last refocusing RF pulse and the acquisition centre. Another, less favorable, option would be to replace all refocusing RF pulses with shaped RF pulses combined with corresponding slice-selection gradient pulses. This approach would also reduce the maximum achievable AC frequency because shaped RF pulses would occupy a significant portion of the inter-RF pulse intervals, so that not much time would remain for the application of electric pulses. If electric pulses were applied simultaneously with the shaped RF pulses then this would not pose such a hard limit.

6. Conclusion

Current density imaging methods can be used to image current selectively according to the charge mobility. The three CDI sequences presented in this work can efficiently distinguish between resistive current of mobile ions and capacitive current of fixed ions and can selectively image resistive (DC-CDI), capacitive (AC–DC-CDI) or both (AC-CDI) current components. The time average of the capacitive current component increases with increasing current frequency, while the resistive current component remains unchanged. Therefore, it is important to use alternating current of sufficiently high frequency for successful detection of capacitive current. This is especially true in biological samples where the decay rates of capacitive currents are fast. Future developments in the current-type selective CDI techniques may allow the use of higher AC frequencies than the presently used 500 Hz and thus improve the performance of CDI experiments on biological samples. The presented CDI methods offer a new MRI contrast mechanism that depends on ion mobility of the samples.

Acknowledgment

The author thanks Andrej Pintar for proofreading the manuscript.

References

[1] Y. Manassen, E. Shalev, G. Navon, Mapping of electrical circuits using chemical-shift imaging, J. Magn. Reson. 76 (1988) 371–374.
[2] M. Joy, G. Scott, M. Henkelman, In vivo detection of applied electric currents by magnetic resonance imaging, Magn. Reson. Imaging 7 (1989) 89–94.
[3] A.T. Basford, J.R. Basford, J. Kugel, R.L. Ehman, Lorentz-force-induced motion in conductive media, Magn. Reson. Imaging 23 (2005) 647–651.
[4] I. Sersa, O. Jarh, F. Demsar, Magnetic resonance microscopy of electric currents, J. Magn. Reson. A111 (1994) 93–99.
[5] U. Mikac, F. Demsar, K. Beravs, I. Sersa, Magnetic resonance imaging of alternating electric currents, Magn. Reson. Imaging 19 (2001) 845–856.
[6] G.C. Scott, M.L. Joy, R.L. Armstrong, R.M. Henkelman, RF current density imaging in homogeneous media, Magn. Reson. Med. 28 (1992) 186–201.
[7] F.A. Duck, Physical Properties of Tissue: A Comprehensive Reference Book, Academic Press, London, 1990.
[8] K.R. Foster, H.P. Schwan, Dielectric properties of tissues and biological materials: a critical review, Crit. Rev. Biomed. Eng. 17 (1989) 25–104.
[9] B. Buhai, T. Binser, R. Kimmich, Electroosmotic flow, ionic currents, and pressure-induced flow in microsystem channel networks: NMR mapping and computational fluid dynamics simulations, Appl. Magn. Reson. 32 (2007) 25–49.
[10] B. Buhai, R. Kimmich, Dissimilar electro-osmotic flow and ionic current recirculation patterns in porous media detected by NMR mapping experiments, Phys. Rev. Lett. 96 (2006) 174501.
[11] M. Weber, R. Kimmich, Maps of electric current density and hydrodynamic flow in porous media: NMR experiments and numerical simulations, Phys. Rev. E: Stat. Nonlin. Soft Matter Phys. 66 (2002) 026306.
[12] E. Kossel, M. Weber, R. Kimmich, Visualization of transport: NMR microscopy experiments with model objects for porous media with pore sizes down to 50 micron, Solid State Nucl. Magn. Reson. 25 (2004) 28–34.
[13] U. Mikac, A. Demsar, F. Demsar, I. Sersa, A study of tablet dissolution by magnetic resonance electric current density imaging, J. Magn. Reson. (2006).
[14] K. Beravs, P. Oven, I. Serša, N. Torelli, F. Demšar, Electric current density imaging of pedunculate oak (*Quercus robur* L.) twigs by magnetic resonance imaging, Holzforschung 52 (1998) 541–545.
[15] R.S. Yoon, T.P. DeMonte, K.F. Hasanov, D.B. Jorgenson, M.L. Joy, Measurement of thoracic current flow in pigs for the study of defibrillation and cardioversion, IEEE Trans. Biomed. Eng. 50 (2003) 1167–1173.
[16] D. Miklavcic, K. Beravs, D. Semrov, M. Cemazar, F. Demsar, G. Sersa, The importance of electric field distribution for effective in vivo electroporation of tissues, Biophys. J. 74 (1998) 2152–2158.
[17] K. Beravs, D. White, I. Sersa, F. Demsar, Electric current density imaging of bone by MRI, Magn. Reson. Imaging 15 (1997) 909–915.
[18] A. Patriciu, K. Yoshida, J.J. Struijk, T.P. DeMonte, M.L. Joy, H. Stodkilde-Jorgensen, Current density imaging and electrically induced skin burns under surface electrodes, IEEE Trans. Biomed. Eng. 52 (2005) 2024–2031.
[19] K. Beravs, R. Frangez, F. Demsar, Specific absorption rate study for radiofrequency current density imaging using a two-dimensional finite element model, Magn. Reson. Med. 44 (2000) 610–615.
[20] M.L. Joy, V.P. Lebedev, J.S. Gati, Imaging of current density and current pathways in rabbit brain during transcranial electrostimulation, IEEE Trans. Biomed. Eng. 46 (1999) 1139–1149.
[21] R.S. Yoon, A. Czaya, H.C. Kwan, M.L. Joy, Changes in the complex permittivity during spreading depression in rat cortex, IEEE Trans. Biomed. Eng. 46 (1999) 1330–1338.
[22] Y. Ider, O. Birgul, Use of magnetic fields generated by the internal distribution of injected currents for electrical impedance tomography (MR-EIT), Elektrik 6 (1998) 215–225.
[23] S.H. Oh, J.Y. Han, S.Y. Lee, M.H. Cho, B.I. Lee, E.J. Woo, Electrical conductivity imaging by magnetic resonance electrical impedance tomography (MREIT), Magn. Reson. Med. 50 (2003) 875–878.
[24] T. Gullion, D.B. Baker, M.S. Conradi, New, compensated Carr–Purcell sequences, J. Magn. Reson. 89 (1990) 479–484.
[25] I. Sersa, Auxiliary phase encoding in multi spin-echo sequences: application to rapid current density imaging, J. Magn. Reson. 190 (2008) 86–94.
[26] C.H. Hamann, A. Hamnett, W. Vielstich, Electrochemistry, Wiley-VCH, Weinheim, New York, 1998.
[27] C. Gabriel, T.Y. Chan, E.H. Grant, Admittance models for open ended coaxial probes and their place in dielectric spectroscopy, Phys. Med. Biol. 39 (1994) 2183–2200.
[28] S. Meiboom, D. Gill, Modified spin-echo method for measuring nuclear relaxation times, Rev. Sci. Instrum. 29 (1958) 688–691.